Image Reconstruction in Electrical Impedance Tomography Based on Structure-Aware Sparse Bayesian Learning

Image Reconstruction in Electrical Impedance Tomography Based on Structure-Aware Sparse Bayesian Learning

Shengheng Liu, *Member, IEEE*, Jiabin Jia, *Member, IEEE*, Yimin D. Zhang, *Senior Member, IEEE*, and Yunjie Yang, *Member, IEEE*

Abstract—Electrical impedance tomography (EIT) is developed to investigate the internal conductivity changes of an object through a series of boundary electrodes, and has become increasingly attractive in a broad spectrum of applications. However, the design of optimal tomography image reconstruction algorithms has not achieved the adequate level of progress and matureness. In this paper, we propose an efficient and high-resolution EIT image reconstruction method in the framework of sparse Bayesian learning. Significant performance improvement is achieved by imposing structure-aware priors on the learning process to incorporate the prior knowledge that practical conductivity distribution maps exhibit clustered sparsity and intra-cluster continuity. The proposed method not only achieves high-resolution estimation and preserves the shape information even in low signal-to-noise ratio scenarios, but also avoids the time-consuming parameter tuning process. The effectiveness of the proposed algorithm is validated through comparisons with state-of-the-art techniques using extensive numerical simulation and phantom experiment results.

Index Terms—Inverse problem, electrical impedance tomography (EIT), sparse Bayesian learning (SBL), image reconstruction, maximum *a posteriori* (MAP) estimation.

I. INTRODUCTION

ELECTRICAL impedance tomography (EIT) is a promising non-invasive imaging modality for continuous real-time visualization of the dynamic electric conductivity distribution of the interior of a body. To perform EIT, we apply weak low-frequency alternating currents (the typical frequency range is 1–$100\,\mathrm{kHz}$ and the magnitude is 1–$5\,\mathrm{mA}$) in multiple manners and measure the corresponding peripheral voltages through an array of electrodes attached on the surface of an object. Then, the cross-sectional image of the internal spatial conductivity distribution is recovered from the resulting boundary voltage measurements. Despite its relatively low spatial resolution ($\sim 10\%$ of the sensor diameter) that hinders its general applicability, EIT has become

a well-accepted tomographic imaging technique because of its desirable properties of portability, low cost, no known hazards, and high temporal resolution in comparison with other techniques available for probing internal dynamics. As a result, EIT finds broad applications in a number of fields, such as industrial process monitoring [2]–[4], geophysical exploration [5]–[7], and biomedical diagnosis [8]–[10].

Mathematically, the reconstruction of conductivity maps in EIT amounts to solving a nonlinear ill-posed inverse problem from noisy data. Regularization techniques can be employed to mitigate the instability of the solutions. One of the most widely used families is the one-step Gauss–Newton (GN) reconstruction approach [11], which allows the use of sophisticated regularized models to describe the EIT inverse problem through a heuristically determined prior [12], [13]. Landweber iteration is a variation of the steepest gradient descent method and is also widely used in EIT [14], [15]. The algebraic reconstruction technique (ART) is a simple and effective image reconstruction method for computerized tomography that can be applied to EIT [16], [17]. Other important methods include regularization via the total variation (TV) functional [18], [19], which allows image reconstruction with edge preservation.

As EIT solutions generally manifest themselves as sparse vectors, a number of sparse regularization approaches have been proposed to stabilize the inversion. For example, in [20]–[22], an ℓ_1 penalty was incorporated into the regularization to promote sparsity. It is shown in [23] that, by clustering relevant signal components together and taking the dependencies between them into account, a superior performance is achieved through the exploitation of structure-based approaches in various practical scenarios. On this basis, sparse signal recovery algorithms have been developed in the literature to exploit the cluster structure of the signals. These methods generally require certain knowledge about the signals, such as the size and distribution of the partition, and the number of nonzero entries of the signal to be recovered. In many applications, however, such knowledge is unavailable. In [24], an adaptive group sparsity (AGS) constraint is proposed to obtain enhanced image quality, where the required *a priori* knowledge is first obtained through a coarse image reconstruction, and images with a finer quality are then obtained.

A natural mechanism to incorporate the structure knowledge in solving the inverse problem is to employ Bayesian approaches [25], [26], which are aimed to characterize the posterior distribution, e.g., computing posterior moments or other

posterior expectations. Sampling via Markov chain Monte Carlo (MCMC) [27] techniques is among the most commonly used paradigms for Bayesian inversion. Although various efforts have been made to accelerate the MCMC approach by exploiting, for example, the gradient and Hessian information of the posterior density [28], or multilevel sampling strategies [29], generating sufficient MCMC samples is still computationally costly [26]. Alternatively, we can use the filtering and variational methods, which provide approximations of the exact posterior by finding the best representative from a class of simpler distributions. Readers are referred to [26] and the references therein for an overview.

The past few years have witnessed extensive research and a significant progress on Bayesian inversion in terms, e.g., of the design of correlation priors and the use of hierarchical models. To name a few, in [30], a Bayesian hierarchical model with conditionally Gaussian priors was used to resolve piecewise smooth structures in noisy and blurred images. In [31], a unified and efficient Bayesian method based on Krylov subspace iterative techniques and preconditioners was further derived to compute the approximated maximum *a posteriori* (MAP) estimate of the image and the prior variance. The algorithm proposed in [31] was later successfully applied to cerebral source localization [32], where the variances are assumed to be guided by a hyperprior with the form of generalized Gamma family, so as to favor small values while permitting rare large outliers which correspond to high source amplitudes. Besov space priors [33] defined by a wavelet expansion with random coefficients have attracted broad attention in the medical imaging community due to their merits such as edge-preserving, sparsity-promoting, and discretization invariant, with imaging results similar to TV regularization [33]–[35]. In [36], the smoothness of unknown targets is modelled by Whittle-Matérn fields, which are essentially stationary Gaussian random fields specified by a correlation function to control the anisotropic properties of the prior distribution. A finite-dimensional approximation of the Whittle-Matérn priors is derived from sparse inverse covariance matrices by using a stochastic partial differential equation. The problem considered in [37] is to reconstruct the conductivity consisting of well-defined inclusion-type targets in an approximately homogeneous background. The proposed iterative algorithm is based on the use of a nonlinear edge-preferring prior density and the minimization of the corresponding Tikhonov functional by efficiently solving an approximate sequence of linearized problems with the help of prior-conditioning and least squares with QR factorization (LSQR). In [38], the inverse problem of magnetoencephalography (MEG), which is very similar to EIT, is solved by postulating a hierarchical conditionally Gaussian prior model, where an anatomical prior is introduced to reflect the direction preference of each dipole based on the *a priori* magnetic resonance imaging (MRI) information. The hyperparameter vector consists of prior variances of the dipole moments, which are assumed to follow a non-conjugate gamma distribution with variable scaling and shape parameters. By combining the iterative alternating sequential algorithm with Krylov subspace iterative solver, satisfactory sparsity control and convergence rate are both achieved.

The recently proposed sparse Bayesian learning (SBL) framework [39]–[44], which is closely related to the term automatic relevant determination (ARD) in the context of neural network, can adaptively and flexibly explore and exploit signal structures such as clustering or continuity without any *a priori* information. In addition, SBL is more advantageous than other families of aforementioned algorithms in the sense that it is more robust in noisy environments, and offers better performance when the columns of the dictionary matrix are highly correlated and/or the image to be reconstructed is not highly sparse [39]. In this paper, therefore, we introduce the concept of structure-aware sparse Bayesian learning (SA-SBL) to perform EIT imaging, and both the clustered sparsity and intra-cluster correlation are utilized in the image reconstruction to achieve improved reconstruction accuracy. Compared with the state-of-the-art methods, the proposed approach is advantageous because its structure-aware modeling capability promotes clustered sparsity and eliminates irrelevant components. In addition, the proposed method yields a better approximation to the ℓ_0-norm sparsity measure and, as a result, achieves enhanced EIT imaging with a higher spatial resolution and improved robustness against Gaussian noise.

The paper is organized as follows. The forward and inverse models are briefly described in Section II. In Section III, we first propose the SA-SBL algorithm for EIT image reconstruction. In Section IV, numerical and real data experiments are designed to simulate the challenging medical application scenarios, and the performance of the proposed algorithms is compared with other state-of-the-art approaches. The paper is concluded in Section V.

Notations: Lower-case (/upper-case) bold characters are used to denote vectors (/matrices). $\overline{(\cdot)}$ and $|\cdot|$ respectively return the average of a given vector and the modulus of a given complex number. ∇ is the Nabla symbol. $\mathrm{diag}\{\mathbf{A}\}$ returns a column vector consisting of the main diagonal entries, whereas and $\mathrm{diag}\{\mathbf{A}, 1\}$ returns one corresponding to the first-diagonal entries above the main diagonal. $\mathbf{I}_N$ denotes an $N \times N$ identity matrix. $\mathrm{tr}(\cdot)$ and $(\cdot)^{\mathrm{T}}$ respectively represent the trace and transpose operation of a matrix. $\|\cdot\|_p$ represents the ℓ_p-norm of a vector. $\mathbb{E}(\cdot)$ returns the expected value of a discrete random variable. $p(\cdot)$ denotes the probability density function. $\mathcal{N}(\cdot)$ denotes Gaussian distribution. $\mathbb{R}$ is the set of real numbers.

II. SIGNAL MODEL

A. Forward Model

In EIT, the computation of the voltage measurements from the known currents and conductivity distribution is referred to as the forward problem. The EIT forward model is mathematically established from a low-frequency approximation of a subset of the Maxwell's electromagnetic equations with some mixed Dirichlet/Neumann boundary conditions [45]. Consider a bounded domain Ω with piecewise smooth boundary $\partial\Omega$. Let σ denote the real-valued conductivity distribution in Ω. Assume that the boundary electrodes are perfectly conductive. Then, applying a current flux through these electrodes results in the scalar interior electric potential u characterized as the solution to

$$\nabla \cdot (\sigma \nabla u) = 0 \quad \text{in } \Omega, \tag{1}$$

where we assume that the static excitation condition is satisfied and no current sources/sinks exist within Ω. The complete electrode model (CEM) is the most accurate model for EIT since it accounts for the effects of the electrodes and the contact impedances between the electrolyte and the electrodes [47]. Assume that a total of L electrodes are attached to the boundary $\partial\Omega$, whose locations are denoted as $\partial\Omega_l \subset \partial\Omega$, $l = 1, 2, \ldots, L$. Denote their contact impedances as z_l. Then, the boundary conditions of the CEM is expressed as [45],

$$u + z_l\sigma\nabla u \cdot \vec{e} = v_l \quad \text{on } \partial\Omega_l, \tag{2}$$

$$\int_{\mathcal{E}_l} \sigma\nabla u \cdot \vec{e} = I_l \quad \text{on } \partial\Omega_l, \tag{3}$$

$$\sigma\nabla u \cdot \vec{e} = 0 \quad \text{on } \partial\Omega \Big/ \bigcup_{l=1}^{L} \partial\Omega_l, \tag{4}$$

where $\vec{e}$ is the outer normal vector on $\partial\Omega$, and I_l denotes the injected current at the l-th electrode.

B. Inverse Model

The inverse problem in EIT is to determine the conductivity in the interior of a object based on the simultaneous measurements of alternating currents and voltages at the boundary. In this paper, linearized difference imaging is considered. By solving the Laplacian elliptic partial differential equation given in (1), we can readily relate the map of internal conductivity perturbation $\delta\boldsymbol{\sigma} \in \mathbb{R}^{N \times 1}$ within the region of interest to its corresponding boundary voltage variation $\delta\mathbf{v} \in \mathbb{R}^{M \times 1}$ ($M \ll N$) using the following linear approximation [46]

$$\delta\mathbf{v} \approx \mathbf{J}\delta\boldsymbol{\sigma} + \mathbf{n}, \tag{5}$$

where $\mathbf{n}$ is the measurement noise vector. In this paper, we assume that the noise vector is additive and follows the zero-mean Gaussian distribution with $\mathbf{n} \sim \mathcal{N}(\mathbf{0}, \gamma_0\mathbf{I})$. Note that, in practice, EIT systems are susceptible to other types of noise and modeling errors. Sources of such noise and errors include multiplicative noise and bias due to amplifier gain distortions and offsets, inter-channel measurement noise due to cross-talk between measurement channels, linearization errors when reference conductive distribution does not match the reference voltages used to compute the Jacobian, and errors in electrode position, domain shape/size and FEM discretization level. However, given the space limitation, it is difficult to examine different types of noise and errors in this work. As a result, we follow the common practice in EIT image reconstruction and assume the additive noise model in (5) with Gaussian distributed entries (see, e.g., [11], [13]–[21]). Still, the above-mentioned annoying noise and errors may co-exist in the real-data experiments in Section IV-B. As shown later, the proposed method performs better in such cases.

The sensitivity map $\mathbf{J} \in \mathbb{R}^{M \times N}$, also frequently referred to as the Jacobian matrix, is determined by mesh, electrode positions, and current injection/measurement protocol. By integrating over the k-th ($k = 1, 2, \ldots, N$) simplex Ω_k from the scalar product of the gradients of the potential fields u that are induced by driving current pattern I_d and measurement

pattern I_m with the finite element method (FEM), $\mathbf{J}$ can be readily computed as [46]

$$\mathbf{J}\{d, m; k\} = \frac{\partial \mathbf{v}_{d,m}}{\partial \boldsymbol{\sigma}_k} = -\int_{\Omega_k} \nabla u(I_d) \cdot \nabla u(I_m)\mathrm{d}\Omega, \tag{6}$$

where $d \neq m \in \{1, 2, \ldots, M\}$ represents the sample index of selected electrode pairs in the m-th measurement under the d-th current pattern. For notational convenience, in the following discussion, we simplify the notations $\delta\boldsymbol{\sigma}$ and $\delta\mathbf{v}$ as $\boldsymbol{\sigma}$ and $\mathbf{v}$, respectively. In this case, (5) is simplified as

$$\mathbf{v} = \mathbf{J}\boldsymbol{\sigma} + \mathbf{n}. \tag{7}$$

This is a typical example of inverse problems, where the task is to reconstruct a signal from observations that are subject to the forward model. Like many other inverse problems, EIT image reconstruction is severely ill-posed and thus is difficult to obtain stable and reliable solutions. Therefore, it is often formulated as the following regularized optimization problem

$$\hat{\boldsymbol{\sigma}} = \min_{\boldsymbol{\sigma} \in \mathbb{R}^{N \times 1}} d(\mathbf{v}, \mathbf{J}\boldsymbol{\sigma}) + \lambda R(\boldsymbol{\sigma}), \tag{8}$$

where $d(\mathbf{v}, \mathbf{J}\boldsymbol{\sigma})$ is the data fidelity term that enforces $\boldsymbol{\sigma}$ to satisfy the observations $\mathbf{v}$, and $R(\boldsymbol{\sigma})$ is a stable operator, or a regularization term which restricts the solution to comply with a predefined model over $\boldsymbol{\sigma}$. The minimization in (8) represents a tradeoff between fitting the data exactly and stabilizing the solution of $\boldsymbol{\sigma}$, which is controlled by the regularization parameter λ. The major problem in this framework is that it is difficult to determine a proper $R(\boldsymbol{\sigma})$ such that it represents a most appropriate model for EIT image reconstruction and, at the same time, its optimization procedure can be easily implemented.

In this work, equation (8) is interpreted in a Bayes perspective such that finding the solution amounts to performing the MAP estimation. In this case, $d(\mathbf{v}, \mathbf{J}\boldsymbol{\sigma})$ takes the form of a log-likelihood whereas $R(\boldsymbol{\sigma})$ takes the form of a parametric log-prior $\log p(\boldsymbol{\sigma}; \Theta)$ over variable $\boldsymbol{\sigma}$. As such, the minimization in (8) becomes [26], [27]

$$\hat{\boldsymbol{\sigma}} = \min_{\boldsymbol{\sigma} \in \mathbb{R}^{N \times 1}} \log p(\mathbf{v}\,|\,\boldsymbol{\sigma}) + \lambda \log p(\boldsymbol{\sigma}; \Theta). \tag{9}$$

This allows for more adequately modeling the *a priori* knowledge about the objective. Compared to the conventional regularization approach based on functional analysis, the Bayesian probabilistic approach provides a more attractive and rational framework for the parameter recovery, as it allows for the quantification of the uncertainty in the recovery, while naturally accommodating different types of data and rich models of *a priori* information.

III. IMAGE RECONSTRUCTION BASED ON SA-SBL

In medical imaging applications, generally, the underlying conductivity distribution change $\boldsymbol{\sigma}$ can be viewed as a concatenation of several clusters due to its inherent clustering structure. In practice, however, the actual clustering partition pattern is more likely to be unknown. In this context, we consider a general case in which all the clusters overlap each other with an equal size h and the nonzero entries are arbitrarily distributed. It was proved in [39] that, since real

clustering partition can be learned during the SBL process by revoking and merging the preset clusters, the reconstruction performance is guaranteed to approach the result obtained from the known clustering partition counterparts. To facilitate the utilization of SA-SBL framework, we factorize $\boldsymbol{\sigma}$ as

$$\boldsymbol{\sigma} \triangleq \boldsymbol{\Psi}\mathbf{x} \triangleq [\boldsymbol{\Psi}_1, \ldots, \boldsymbol{\Psi}_g] \left[\mathbf{x}_1^{\mathrm{T}}, \ldots, \mathbf{x}_g^{\mathrm{T}}\right]^{\mathrm{T}}, \quad (10)$$

where $g = N - h + 1$ is the total number of clusters. In addition, for $\forall i = 1, 2, \ldots, g$, $\mathbf{x}_i = [x_i, \ldots, x_{i+h-1}]^{\mathrm{T}} \in \mathbb{R}^{h \times 1}$ denotes the i-th preset cluster, and $\boldsymbol{\Psi}_i \triangleq \left[\mathbf{0}_{(i-1) \times h}^{\mathrm{T}}, \mathbf{I}_{h \times h}^{\mathrm{T}}, \mathbf{0}_{(N-i-h+1) \times h}^{\mathrm{T}}\right]^{\mathrm{T}} \in \mathbb{R}^{N \times h}$. The underlying linear model in (7) can then be rewritten as

$$\mathbf{v} = \mathbf{J}\boldsymbol{\Psi}\mathbf{x} + \mathbf{n} \triangleq \boldsymbol{\Phi}\mathbf{x} + \mathbf{n}, \quad (11)$$

where $\boldsymbol{\Phi} \triangleq [\boldsymbol{\Phi}_1, \ldots, \boldsymbol{\Phi}_g]$, and $\boldsymbol{\Phi}_i \triangleq \mathbf{J}\boldsymbol{\Psi}_i \in \mathbb{R}^{M \times h}$. We assume that the prior of the weights $\mathbf{x}$ follows a zero-mean Gaussian distribution with

$$p\left(\mathbf{x}; \{\gamma_i, \mathbf{B}_i\}_{i=1}^g\right) = \mathcal{N}\left(\mathbf{0}, \boldsymbol{\Sigma}_0\right), \quad (12)$$

where the stretched covariance matrix is expressed as

$$\boldsymbol{\Sigma}_0 = \begin{bmatrix} \gamma_1 \mathbf{B}_1 & & \mathbf{0} \\ & \ddots & \\ \mathbf{0} & & \gamma_g \mathbf{B}_g \end{bmatrix} \in \mathbb{R}^{gh \times gh}. \quad (13)$$

The structured sparsity in $\mathbf{x}$ is determined by γ_i, $i = 1, \ldots, g$, in $\boldsymbol{\Sigma}_0$. If $\gamma_i = 0$, the values of the entries in the associated i-th cluster of $\mathbf{x}$ becomes zero. By considering the fact that $\mathbf{n} \sim \mathcal{N}(\mathbf{0}, \gamma_0 \mathbf{I})$, the *a posteriori* belief for the weights $\mathbf{x}$ is subject to the following Gaussian distribution

$$p\left(\mathbf{x} \,|\, \mathbf{v}; \Theta\right) = \mathcal{N}\left(\boldsymbol{\mu}_x, \boldsymbol{\Sigma}_x\right), \quad (14)$$

where $\Theta \triangleq \{\gamma_0, \{\gamma_i, \mathbf{B}_i\}_{i=1}^g\}$ denotes the hyperparameters with mean vector

$$\boldsymbol{\mu}_x = \boldsymbol{\Sigma}_0 \boldsymbol{\Phi}^{\mathrm{T}} \left(\gamma_0 \mathbf{I} + \boldsymbol{\Phi}\boldsymbol{\Sigma}_0\boldsymbol{\Phi}^{\mathrm{T}}\right)^{-1} \mathbf{v} \in \mathbb{R}^{gh \times 1}, \quad (15)$$

and covariance matrix

$$\boldsymbol{\Sigma}_x = \left(\boldsymbol{\Sigma}_0^{-1} + \frac{1}{\gamma_0}\boldsymbol{\Phi}^{\mathrm{T}}\boldsymbol{\Phi}\right)^{-1} \in \mathbb{R}^{gh \times gh}$$
$$= \boldsymbol{\Sigma}_0 - \boldsymbol{\Sigma}_0\boldsymbol{\Phi}^{\mathrm{T}}\boldsymbol{\Sigma}_v^{-1}\boldsymbol{\Phi}\boldsymbol{\Sigma}_0, \quad (16)$$

with $\boldsymbol{\Sigma}_v \triangleq \gamma_0 \mathbf{I} + \boldsymbol{\Phi}\boldsymbol{\Sigma}_0\boldsymbol{\Phi}^{\mathrm{T}}$.

The MAP probability estimate of $\mathbf{x}$ is obtained from the posterior mean $\boldsymbol{\mu}_x$, prior to which, the hyperparameters Θ must be estimated first. The expectation-maximization (EM) method is employed to maximize $p(\mathbf{v}; \Theta)$, which is equivalent to minimizing $-\log p(\mathbf{v}; \Theta)$. Thus we obtain the following cost function

$$\mathcal{L}(\Theta) \triangleq -2\log \int p(\mathbf{v}\,|\,\mathbf{x}; \gamma_0) p\left(\mathbf{x}; \{\gamma_i, \mathbf{B}_i\}_{i=1}^g\right) \mathrm{d}\mathbf{x}$$
$$= \log|\boldsymbol{\Sigma}_v| + \mathbf{v}^{\mathrm{T}}\boldsymbol{\Sigma}_v^{-1}\mathbf{v}. \quad (17)$$

The correlation structure matrix $\mathbf{B}_i$ can be updated using the gradient of the cost function with respect to $\mathbf{B}_i$. To avoid

the overfitting problem, we introduce $\widetilde{\mathbf{B}}_i$ as an intermediate variable to compute $\mathbf{B}_i$, which is updated as,

$$\widetilde{\mathbf{B}}_i^{\mathrm{new}} = \widetilde{\mathbf{B}}_i + \frac{1}{\gamma_i}\left(\boldsymbol{\Sigma}_x^i + \boldsymbol{\mu}_x^i\left(\boldsymbol{\mu}_x^i\right)^{\mathrm{T}}\right), \quad (18)$$

where $\boldsymbol{\mu}_x^i = \boldsymbol{\mu}_x\left((i-1)h+1 : ih\right)$, $\boldsymbol{\Sigma}_x^i = \boldsymbol{\Sigma}_x\left((i-1)h+1 : ih, (i-1)h+1 : ih\right)$. The estimation of $\mathbf{B}_i$ is then obtained by constraining it to the following Toeplitz form,

$$\mathbf{B}_i = \mathrm{Toeplitz}\left(\left[r_i^0, r_i^1, \ldots, r_i^{h-1}\right]\right)$$
$$= \begin{bmatrix} r_i^0 & r_i^1 & \cdots & r_i^{h-1} \\ \vdots & \ddots & \ddots & \vdots \\ r_i^{h-2} & \cdots & r_i^0 & r_i^1 \\ r_i^{h-1} & r_i^{h-2} & \cdots & r_i^0 \end{bmatrix}, \quad (19)$$

where

$$r_i = \mathrm{sign}(\tilde{r}_i) \cdot \min\left\{|\tilde{r}_i|, 0.99\right\}, \quad (20)$$

$$\tilde{r}_i = \frac{\overline{\mathrm{diag}(\widetilde{\mathbf{B}}_i, 1)}}{\overline{\mathrm{diag}(\widetilde{\mathbf{B}}_i)}}. \quad (21)$$

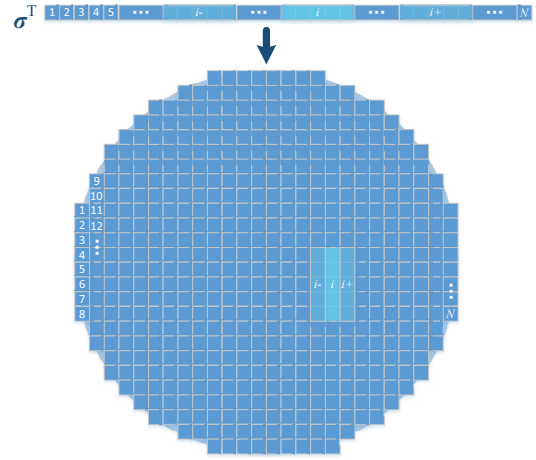Note that the averaging of r_i in the above computation effectively prevents against overfitting.

Fig. 1. Illustration of the structure in the conductivity distribution $\boldsymbol{\sigma}$.

An computationally efficient learning rule for the hyperparameter γ_i can be derived by minimizing the cost function via the majorization-minimization approach [39], [48], which can be expressed as

$$\gamma_i^{\mathrm{new}} = (\gamma_i + \beta\gamma_{i+} + \beta\gamma_{i-}) \cdot \frac{\left\|\sqrt{\mathbf{B}_i}(\boldsymbol{\Phi}_i)^{\mathrm{T}}\boldsymbol{\Sigma}_v^{-1}\mathbf{v}\right\|_2}{\sqrt{\mathrm{tr}\left((\boldsymbol{\Phi}_i)^{\mathrm{T}}\boldsymbol{\Sigma}_v^{-1}\boldsymbol{\Phi}_i\mathbf{B}_i\right)}}, \quad (22)$$

where $\beta \in [0, 1]$ models the pattern coupling between the hyperparameter γ_i of cluster $\mathbf{B}_i$ and the hyperparameters $\{\gamma_{i+}, \gamma_{i-}\}$ of its neighboring clusters, and subscripts $i+$ and $i-$ respectively indicate the neighboring clusters of the i-th cluster with larger and smaller indices. The mapping from vector $\boldsymbol{\sigma}$ to the actual geometry and the neighboring clusters are illustrated in Fig. 1. By introducing parameter β into the

learning process, the relevance of the neighboring clusters, which are not adjacent to the underlying cluster within vector $\boldsymbol{\sigma}$, is also exploited. Note that, while the update formulae provide good numerical behavior in all the experiments, there is no theoretical analysis on the stability of updating rules of $\mathbf{B}_i$ and γ_i. Nevertheless, as EIT has the merit of high time resolution, we can discard the abnormal frames.

By treating $\mathbf{x}$ as a latent parameter, and setting the derivative of the cost function over γ_0 to 0, the learning rule for γ_0 is derived as

$$\gamma_0 = \frac{1}{M} \left(\|\mathbf{v} - \boldsymbol{\Phi}\boldsymbol{\mu}_x\|_2^2 + \sum_{i=1}^{g} \text{tr} \left(\boldsymbol{\Sigma}_x^i (\boldsymbol{\Phi}_i)^{\text{T}} \boldsymbol{\Phi}_i \right) \right). \quad (23)$$

A pseudo-code implementation of the proposed algorithm for EIT image reconstruction is provided in **Algorithm 1**. To update the parameters through the EM approach, the computational complexity of the proposed method is $O(M^2 gh)$ for each iteration. It is worth emphasizing that, the time-consuming parameter tuning process is averted in the proposed algorithm. The concept of pattern coupling was studied in [40], where the recovery performance is shown to be insensitive to the choice of β as long as $\beta > 0$. It was also proved that taking different values of h will lead to negligible difference [39]. For simplicity, we set $\beta = 0.25$ and $h = 4$ throughout this paper. The other two input parameters $\epsilon_{\min}$ and $\vartheta_{\max}$ are related to the algorithm precision and are selected according to the required performance and affordable computational complexity. As such, none of them requires a time-consuming parameter tuning process.

Algorithm 1: EIT image reconstruction based on SA-SBL algorithm.

Input : $\mathbf{v}$, $\mathbf{J}$, h, β, $\epsilon_{\min}$, $\vartheta_{\max}$

Initialize : Set $\epsilon = 1$, $\vartheta = 0$, $\boldsymbol{\mu}_x = \mathbf{0}_{gh \times 1}$,
$\quad\quad \boldsymbol{\Sigma}_x = \mathbf{0}_{gh \times gh}$, $\gamma_i = \mathbf{1}_{g \times 1}$,
$\quad\quad \gamma_0 = 0.01 \times \sqrt{\frac{1}{N-1} \sum_{i=1}^{N} |v_i - \bar{\mathbf{v}}|^2}$,
$\quad\quad \mathbf{B}_i = \text{Toeplitz}([0.9^0, \dots, 0.9^{h-1}])$.

Iterations:

1 **while** $\epsilon > \epsilon_{\min}$ and $\vartheta \le \vartheta_{\max}$ **do**
2 $\quad$ Update $\boldsymbol{\mu}_x$ using (15);
3 $\quad$ Update $\boldsymbol{\Sigma}_x$ using (16);
4 $\quad$ Update γ_i using (22);
5 $\quad$ Update γ_0 using (23);
6 $\quad$ Update $\mathbf{B}_i$ using (18)–(21);
7 $\quad$ $\epsilon = \|\boldsymbol{\mu}_x^{\text{new}} - \boldsymbol{\mu}_x\|_2 / \|\boldsymbol{\mu}_x^{\text{new}}\|_2$;
8 $\quad$ $\vartheta = \vartheta + 1$.
9 **end**

Output : $\hat{\boldsymbol{\sigma}} = \boldsymbol{\Psi}\hat{\boldsymbol{\mu}}_x$

Remarks: The proposed hierarchical Bayesian model allows the estimation of prior parameters in an unsupervised manner, i.e., the proposed algorithm does not require any information regarding either the sparsity or the clustering prior. Rather, improved performance is achieved by adaptively and flexibly exploring and exploiting such signal structures.

IV. RESULTS AND DISCUSSIONS

In this section, we evaluate the performance of the proposed SA-SBL based method through extensive numerical simulations and phantom experiments. To demonstrate the superiority of the proposed method, comparisons with existing state-of-the-art approaches, such as ART [16], TV regularization [18], ℓ_1 regularization [21], Nissinen's Bayesian method [49], and AGS constraint method [24], are provided. Note that since modeling errors are not considered in this work, the term "Nissinen's Bayesian method" here refers to the conventional MAP estimate without the approximation error method (c.f., Section 2.1 in [49] or Section 2.2.3 in [50]). Note that in terms of the spatial resolution of the reconstructed images, existing Bayesian inversion based methods do not show significant improvement when compared to traditional deterministic approaches. For instance, the reconstructed results using Bayesian inversion with Whittle-Matérn priors are comparable to the solution of the gradient-based smoothness methods [36]. It was also pointed out in [31] that the TV and Perona-Malik regularization schemes can both be seen as MAP estimations of Bayesian hierarchical models proposed therein. As discussed in [50] and will be presented later, Nissinen's Bayesian method demonstrates similar performance with the Tikhonov regularization.

A. Synthetic Data Experiments

We present several synthetic data experiments in this subsection to demonstrate the effectiveness of the proposed algorithm in comparison with other state-of-the-art approaches. In the COMSOL Multiphysics® environment, we design a 16-electrode EIT sensor as shown in Fig. 2(a). The diameter of the sensor is set as 95 mm. As the neighboring bipolar pattern is adopted, the degrees of freedom of the measurement is $M = 16 \times (16-3)/2 = 104$ (dimension of the voltage data vector).
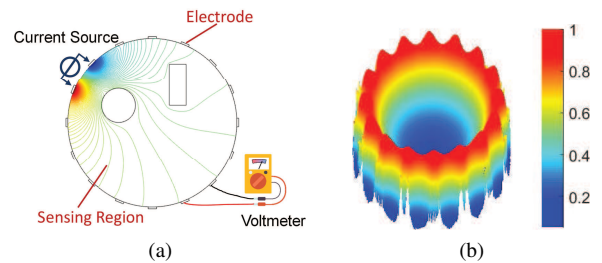

Fig. 2. Synthetic data experimental settings. (a) Schematic illustration of the designed EIT sensor system in the COMSOL environment. (b) Normalized sensitivity map of the EIT sensor configuration.

Based on the sensor configuration, the sensitivity map $\mathbf{J}$ can be computed. The scaled summation of each row of $\mathbf{J}$ is plotted in Fig. 2(b). The sensitivity map is essentially the superposition of all the sensitivity distributions corresponding to each measurement, which is nonuniform as shown in Fig. 2(b). The matrix $\mathbf{J}$ has the highest sensitivity in the pixels near the measurement surface, and becomes less sensitive in the center area. In the linearized algorithm, the sensitivity map directly affects the quality of the reconstructed image,

as the objects near the excitations will be greatly augmented. This will be demonstrated in the following experiments. The mutual coherence [51], $\Xi(\mathbf{J})$, of the matrix $\mathbf{J}$ is defined as the maximum absolute value of the inner product between any two normalized columns $\mathbf{j}_i$ and $\mathbf{j}_k$, i.e.,

$$\Xi(\mathbf{J}) = \max_{1 \leq i,k \leq N, i \neq k} \left\{ \frac{|\mathbf{j}_i^\mathrm{T}\mathbf{j}_k|}{\|\mathbf{j}_i\|_2\|\mathbf{j}_k\|_2} \right\}. \tag{24}$$

The mutual coherence $\Xi(\mathbf{J})$ is an important measure in the field of sparse representations that characterizes the spread of the columns of matrix $\mathbf{J}$. $\Xi(\mathbf{J})$ takes values within the range of $0 \leq \Xi \leq 1$, with a lower value indicating a large spread and a low coherence. For the data being simulated, the mutual coherence of the sensitivity matrix is $\Xi(\mathbf{J}) = 0.9995$, which indicates a high coherence between the columns of matrix $\mathbf{J}$. Under this condition, the SBL algorithm in [39] has been proved effective. The SA-SBL algorithm proposed in the paper is devised through modifications of the SBL algorithm in [39] and provides reliable image reconstruction even when the sensitivity matrix $\mathbf{J}$ is highly coherent.

In this paper, we assume that the voltage data is corrupted by a white Gaussian noise, and we define SNR as

$$\mathrm{SNR} \triangleq 10 \log_{10} \left(\frac{\|\mathbf{v}\|_2^2}{\mathbb{E}\left(\|\mathbf{n}\|_2^2\right)} \right). \tag{25}$$

In this subsection, since we have the ground truth of the conductivity distribution for the synthetic data, the correlation coefficient and the relative reconstruction error can be defined respectively as follows to quantitatively evaluate the reconstruction accuracy [13]:

$$\mathrm{Cor} = \frac{\sum_{i=1}^{N}(\boldsymbol{\sigma}_i - \bar{\boldsymbol{\sigma}})(\boldsymbol{\varsigma}_i - \bar{\boldsymbol{\varsigma}})}{\sqrt{\sum_{i=1}^{N}(\boldsymbol{\sigma}_i - \bar{\boldsymbol{\sigma}})^2 \sum_{i=1}^{N}(\boldsymbol{\varsigma}_i - \bar{\boldsymbol{\varsigma}})^2}}, \tag{26}$$

and

$$\mathrm{Err} = \frac{\|\boldsymbol{\sigma} - \boldsymbol{\varsigma}\|_2}{\|\boldsymbol{\varsigma}\|_2}, \tag{27}$$

where $\boldsymbol{\varsigma}$ represents the true conductivity variation, and the number of simplexes in the inverse FEM mesh is $N = 3228$ in our phantom test. Note that to make the simulation more realistic and to avoid committing an *inverse crime*, we utilize a forward mesh consisting of 6570 domain elements and 304 boundary elements. The adopted forward and inverse FEM meshes are shown in Fig. 3. It can be observed from Fig. 3 that, the inverse mesh consists of square simplices, while the forward mesh consists of triangular simplices. We construct the EIT forward model using the dense mesh, where the electric field potential of each triangular simplex is derived from the values of its corresponding vertices. On the other hand, the conductivity of each square simplex is determined by the conductivity at the center of the square simplex. Thus, the inverse mesh used when solving the inverse problem is totally different from the forward mesh used when generating the measurement data.
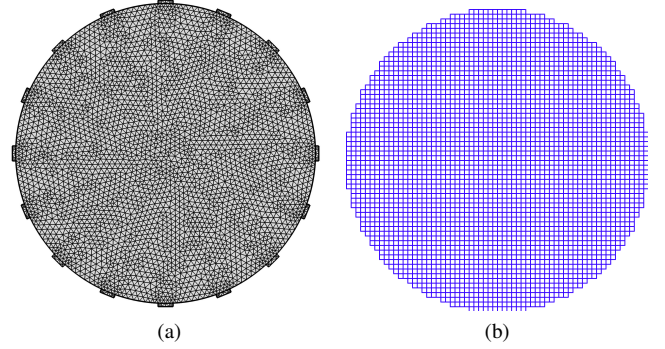

Fig. 3. Adopted forward and inverse FEM meshes. (a) Forward mesh consisting of 6570 domain elements and 304 boundary elements. (b) Inverse mesh consisting of 3228 elements.

First, an illustrative example is presented to evaluate the performance of the proposed method when resolving multiple small objects. As shown in Fig. 4, we design a phantom consisting of three small titanium beta-21S squares with a conductivity value of 7.407×10^5 S/m and a side length of 10 mm, and the conductivity of the background saline is 0.05 S/m. Other simulation settings include an excitation frequency of 10 kHz and a peak-to-peak amplitude of 1.5 mA. The iteration termination conditions for the iterative methods are set to $\epsilon_{\min} = 1 \times 10^{-5}$ and $\vartheta_{\max} = 200$. The target objective parameter in the ℓ_1 regularization is set as 0.1. The iteration step of TV regularization is set as 0.01. For AGS constraint method, the maximum diameter of the group is set as 6 pixels, and the penalty vector is tuned to $\left[\frac{1}{104}, \frac{5}{104}\right]$. All the above simulation settings remains unchanged unless otherwise stated.
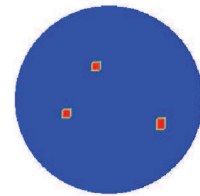

Fig. 4. Ground truth of the generated multiple small objects.

The reconstruction results are given in Table I, where the plots in each row show the results for a different method, whereas each column depicts the results corresponding to different input SNR values. Concretely, in the first three rows of Table I, the boundary between the two closer squares are not clearly resolved. However, compared with the other two methods, Nissinens Bayesian method yields a slightly better resolution. The methods whose results are provided in the last three rows of Table I take the signal sparsity into consideration. However, noticeable artifacts between the pair of close squares can still be observed with the ℓ_1 regularization approach, and the performance degrades significantly when the input SNR is low. Both the AGS constraint method and the proposed SA-SBL based method clearly resolve all three objects, and the results are insensitiveness to the input SNR. Nevertheless, the proposed approach better preserves the edge and shape

TABLE I
ILLUSTRATIVE EXAMPLES OF EIT IMAGE RECONSTRUCTION OF MULTIPLE SMALL OBJECTS.
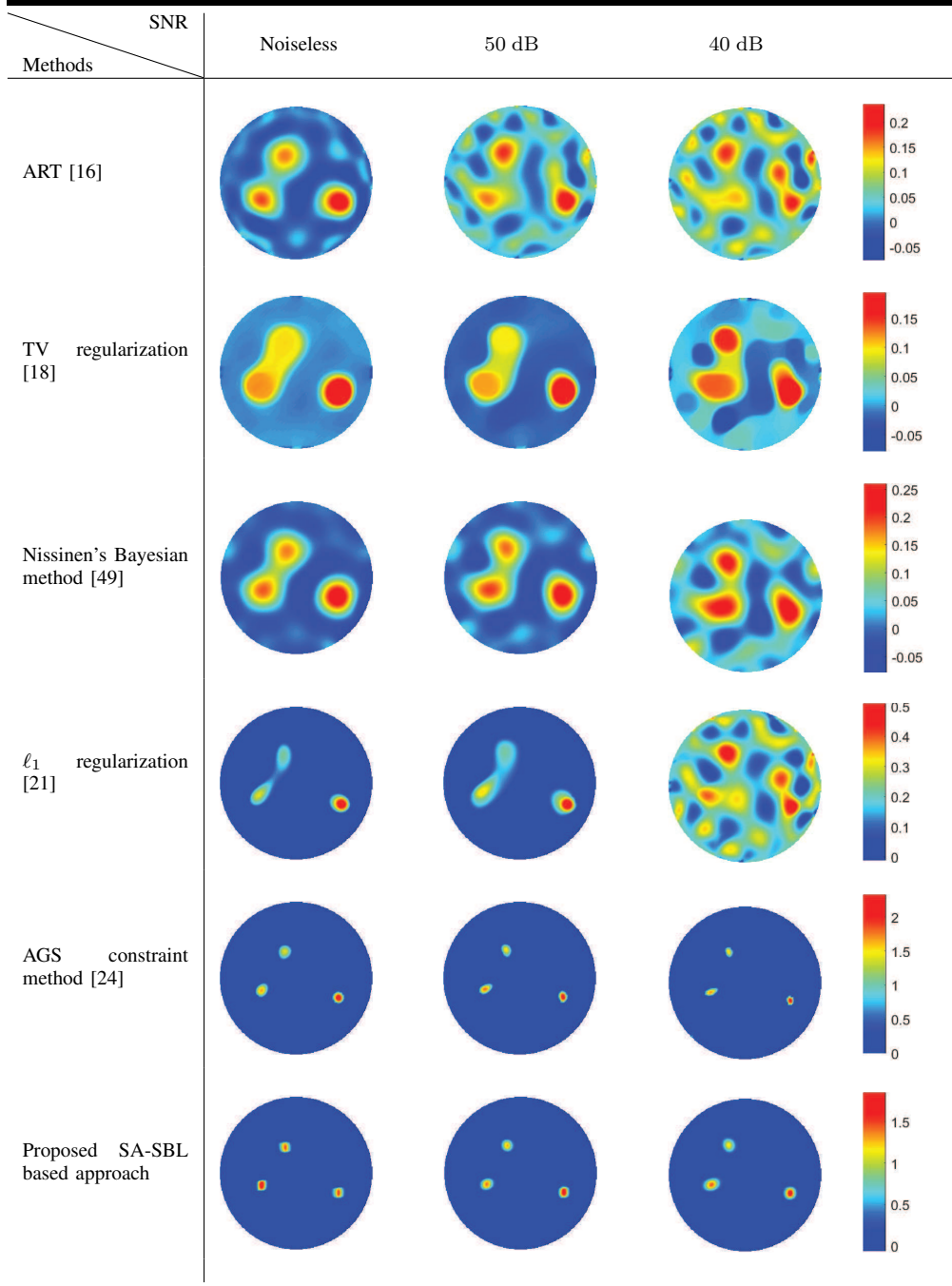
of each object. For the listed iterative algorithms, convergence respectively occurs at approximately 150, 30, 10, 70, 150, and 30 iterations, following the order of appearance in Table I. The following statistical comparison results further demonstrate the advantages of the proposed SA-SBL technique in terms of the correlation coefficient and the relative reconstruction error.

We evaluate the statistical performance through 1,000 Monte Carlo trials with the input SNRs ranging from 35 dB to 70 dB. In Fig. 5, the comparisons are made with respect to different input SNR values for different approaches. In addition to the methods examined in Table I, we also included

the SBL approach exploited in our previous work [1] for comparison. From Fig. 5 we can observe that the AGS, SBL, and SA-SBL based approaches significantly outperform all the others, as can be also seen from Table I. It is worth emphasizing that, the mathematical model of the Bayesian algorithm [49] can be derived equivalently to that of the damped least-square algorithm [53], which is essentially a generalized Tikhonov regularization approach. Hence, as expected, they demonstrate similar performance in reconstruction. Since the method in this paper is developed on the basis of our previous work in [1], we place more emphasis on the comparison

between AGS and SA-SBL based EIT image reconstruction. As the grouping in AGS method is based on the estimated conductivity distribution by the one-step Gaussian Newton solver with Laplacian regularization, which is sensitive to noise, the performance of AGS degrades when the input SNR is low. In addition, the AGS method requires troublesome parameter tuning in practice because different types of weights are assigned when handling the conductivity distribution with different extents of sparsity. Therefore, the proposed SA-SBL based method is advantageous to the AGS constraint method from both performance and implementation perspectives.

In the following, we demonstrate the superiority of the proposed method in terms of the image resolution. We consider a more complicated scenario, which has not been discussed in the existing literature. Extracellular impedance sensing is a feasible technique in the biomedical field to detect morphological changes, membrane permeability, and viability of the cell spheroids. This technique avoids the use of labels, does not interfere with normal cellular behavior *in vitro*, and allows real-time monitoring of cell spheroids [54]. In the initial stages of the transfection or protein/organelle extraction procedures, certain nonionic surfactants, such as Triton X-100 in a proper concentration level, is widely adopted to permeabilize the living cell membrane [55]. As the cell membranes generally show electrically insulating effect at low frequencies, and the impedance of sensor electrodes is fairly sensitive to any changes in the permeability and morphology of membranes and the adherent layers, a remarkable decrease in the conductivity of the outer layers of the cell spheroids will be induced as the result of the utilization of nonionic surfactants [54].

To evaluate the performance of the proposed approach in this challenging scenario, a phantom with a ring shape conductivity distribution is designed in the COMSOL Multiphysics® environment. The ground truth of the synthetic phantom is illustrated in Fig. 6(a). The radii of the inner and outer circles are 10 mm and 25 mm, respectively, and the conductivity values of the inner and outer regions are 0.1 S/m and 0.8 S/m, respectively. For AGS constraint method, the maximum diameter of the group is set as 8 pixels, and the penalty vector is tuned to $\left[\frac{1}{104}, \frac{2}{104}\right]$. Since it has been shown in Table I and Fig. 5 that AGS and the proposed SA-SBL based methods significantly outperform the other approaches, we only provide the results for these two methods together with another commonly used sparsity-based methods, i.e., ℓ_1 regularization method. The result shown in Fig. 6(b) fails to faithfully render the structure: the reconstructed conductivity distribution is overly sparse and inaccurate. By contrast, the ring-shaped structure is recovered with a high fidelity by using the AGS and SA-SBL based methods, as depicted in Figs. 6(c) and (d). Between these two methods, the results reconstructed from the proposed SA-SBL based method clearly exhibit a better accuracy.

B. Real Data Experiments

The performance of the proposed SA-SBL based EIT reconstruction algorithm is further validated through real data experiments in this section. The real data experiments are
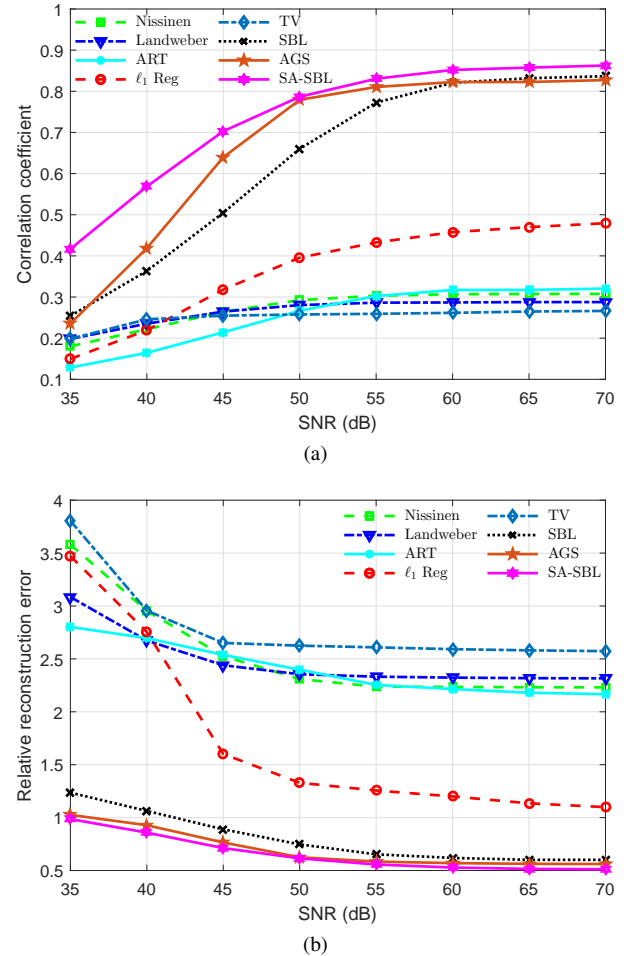

Fig. 5. Comparisons of Monte Carlo trial statistics among different methods. (a) Correlation coefficient. (b) Relative reconstruction error.
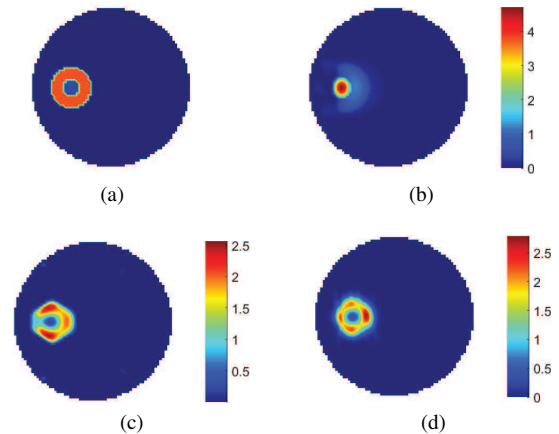

Fig. 6. Ring-shape conductivity image reconstruction test: (a) Ground truth; (b) ℓ_1 regularization; (c) AGS constraint method; (d) Proposed SA-SBL based approach.

designed to visualize the complex flow motions inside a certain boundary, which provides a feasible solution for the monitoring of the cerebral blood flow (CBF) and diagnosis of encephalopathy such as cerebral hemorrhagic stroke. CBF is an important parameter indicating cerebrovascular pathology and neural activities of the human brain. Existing techniques

such as computed tomography (CT) and MRI provide global brain imaging but only show stationary snapshots rather than continuous monitoring. Positron emission tomography (PET) produces three-dimensional brain functional images with a temporal resolution around 30–40 seconds and involves the use of radioactive material. A fast, portable and cost-effective diagnostic imaging modality to monitor the CBF is highly desirable. Since the electrical conductivity of blood is three to four times higher than the electrical conductivity of the brain tissue [56], brain impedance is sensitive to variations of the CBF. Based on this fact, EIT has been utilized in the neuroimaging field. For instance, strong evidences for EIT detection of the cerebral hemodynamic response to the neural stimulus has been demonstrated in [8], [57], [58].

It is worth pointing out that studies in image reconstruction are still at an early stage currently and applications in practical biomedical scenarios are far more complicated than laboratory environment with simplified models and assumptions. Particularly, when imaging a real human head using scalp electrodes, the poorly conducting skull and other extracerebral layers limit the injected current to flowing into the brain compartment [59], [60], and a large proportion of the current is shunted through the scalp [9], [61]. Therefore, the sensitivity of EIT to small intracranial conductivity changes is substantially reduced, making the image reconstruction susceptible to noise and, thus, the inverse problem becomes even more ill-posed [61]. This phenomenon is termed as *blurring effect* [60]. In addition, the obtainable signal amplitude is limited as the injected current is constrained by medical safety regulations [62]. The situation is compounded by the *mismodeling effect* [62], since errors in the shape/size of the electrodes/boundary, in the electrode positions, and in the skin-to-electrode contact impedance can produce artifacts in the reconstructed images [63]. In this paper, we are dealing with one of the most important limitations of the EIT modality, i.e., the *partial volume effect* [60] induced by the low spatial resolution. This has long been a major factor that hinders the practical application of EIT. As such, other aforementioned potential difficulties encountered in practical applications are beyond the scope of this paper and will be addressed in our future work. The objective of this section is to demonstrate the improved spatial resolution by SA-SBL and explore its feasibility in practical medical imaging by conducting experiments in a cylindrical vessel.

Fig. 7. Experimental EIT measurement system.

The experimental setup comprises a cylindrical vessel with an inner diameter of 287 mm. A circular section of the vessel (71 mm from the bottom) is fitted with 16 flush-mounted stainless-steel plate electrodes, each with a contact area of 6 cm^2. These electrodes are wired to an ITS$^{\circledR}$ v5r model EIT system for real-time three dimensional industrial process tomographic imaging. The background substance is saline tap-water with a height of 132 mm during the experiments. Fig. 7 shows the experimental setting of the system. The system supports up to 32 electrodes with a working frequency 10 kHz, and it can deliver up to 650 frames per second (fps) per plane. In the experiment, the current excitation frequency is selected as 10 kHz, and the amplitude of the injected current is 15.17 mA. The adjacent sensing strategy is adopted, and the amplitude data of the boundary voltage is acquired for image reconstruction. The room temperature in the laboratory was 24.8 °C. During the entire experiment process of the experiments, videos are recorded, and the snapshots of these videos are utilized as references to draw comparisons. A piston syringe is used to inject the colored solution into the cylindrical vessel. For both experiments with AGS constraint method, the maximum diameter of the group is set in the range 6 to 11 pixels, and the penalty vector is tuned in the range $\left[\frac{1}{104}, \frac{2}{104}\right]$ to $\left[\frac{1}{104}, \frac{6}{104}\right]$. In the first real-data experiment, the target objective parameter in the ℓ_1 regularization is changed to 0.01.

The first real data experiment is designed to simulate the spurting arterial CBF. By referring to the empirical medical data in [56], we set the conductivities of the red jet ink and the background solution to 0.8 S/m and 0.25 S/m respectively to simulate cerebral blood flow and the rest of brain tissues. For the convenience of the observation and injection, the needle is bent to a right angle and dipped into the water, and the syringe is pressed against the vessel wall. In the first real data experiment, the frame collection rate is set to 125 fps. The 1705-th, 1885-th, 2225-th frames of the collected voltage data are selected to reconstruct the conductivity images of three major stages using different approaches. The results are tabulated in Table II. Note that, the conductivity ratio of the background solution versus the saline ink is low, and the diffusion of the saline ink will lead to a significant reduction in the conductivity. As such, visually visible light-colored ink region can become undetectable if diluted to a certain low concentration. As expected, the best revivification is achieved with the proposed SA-SBL method as shown in the last row of Table II, where the reconstructed high conductivity region most closely resembles the ground truth presented in the first row. In comparison, the reconstructed images with the Nissinen's Bayesian and ℓ_1 regularization methods, respectively depicted in the second and third rows, are either excessively smooth or sparse. In addition, Nissinen's Bayesian method clearly produces more artifacts in the background regions when imaging low contrast objects. The results of the AGS constraint method is shown in the fourth row, where the spatial resolution approaches the proposed SA-SBL. Both the proposed SA-SBL and the AGS constraint methods recovered the image of the needle. However, the AGS constraint method exhibits clear losses in the shape/edge information, and yields

TABLE II
IMAGE RECONSTRUCTION RESULTS OF REAL COLLECTED DATA.

SNR / Methods	Frame 1051	Frame 1451	Frame 2231
Ground truth			
Nissinen's Bayesian method			
ℓ_1 regularization			
AGS constraint method			
Proposed SA-SBL based approach			

very conspicuous artifacts, thus reaffirming the proposed SA-SBL to be the preferred choice.

In the second real data experiment, more complicated flow motions, i.e., the swirl and diffusion are considered. The saline solution of blue jet ink is dripped into the cylindrical vessel from above the top edge of the vessel wall. We set the conductivities of the background solution and the blue solution to 0.014 S/m and 4.21 S/m, respectively. Before the blue solution is dripped, we stir the background tap-water clockwise in advance to ensure that the blue solution drops swirl immediately after they touch the water surface. The frame collection rate is changed to 156 fps. We select one frame from every 50 frames between the 573-rd and the 2223-rd frame. The successive video snapshots and the reconstructed conductivity distribution by using the AGS and SA-SBL methods for the selected frames are shown in Table III. The first two rows are ground truths, the third and fourth

rows are the reconstructed results using the AGS method, and the last two rows are the results of the proposed SA-SBL method. It is observed that the rotation as well as the diffusion motions are recovered with both methods. However, compared with the results obtained by the SA-SBL method, we observe more artifacts and more discontinuities in the recovered ink region by the AGS method. Note that, as the sensitivity map is very sensitive and nonuniform in the near-boundary region of the sensor, which can be seen in Fig. 2(b), in addition to which, both methods are not based on smooth penalty, the reconstructed images close to the vessel wall are likely to suffer from distortion. Nevertheless, as can be observed in Table III, the proposed SA-SBL based method yields higher robustness against such unfavorable factors. It is worth mentioning that, while the contrast between the objects and the background in the synthetic data experiments is high, the results obtained in real data experiments provide a different

TABLE III
SUCCESSIVE RECONSTRUCTED CONDUCTIVITY DISTRIBUTION FRAMES AND GROUND TRUTH.
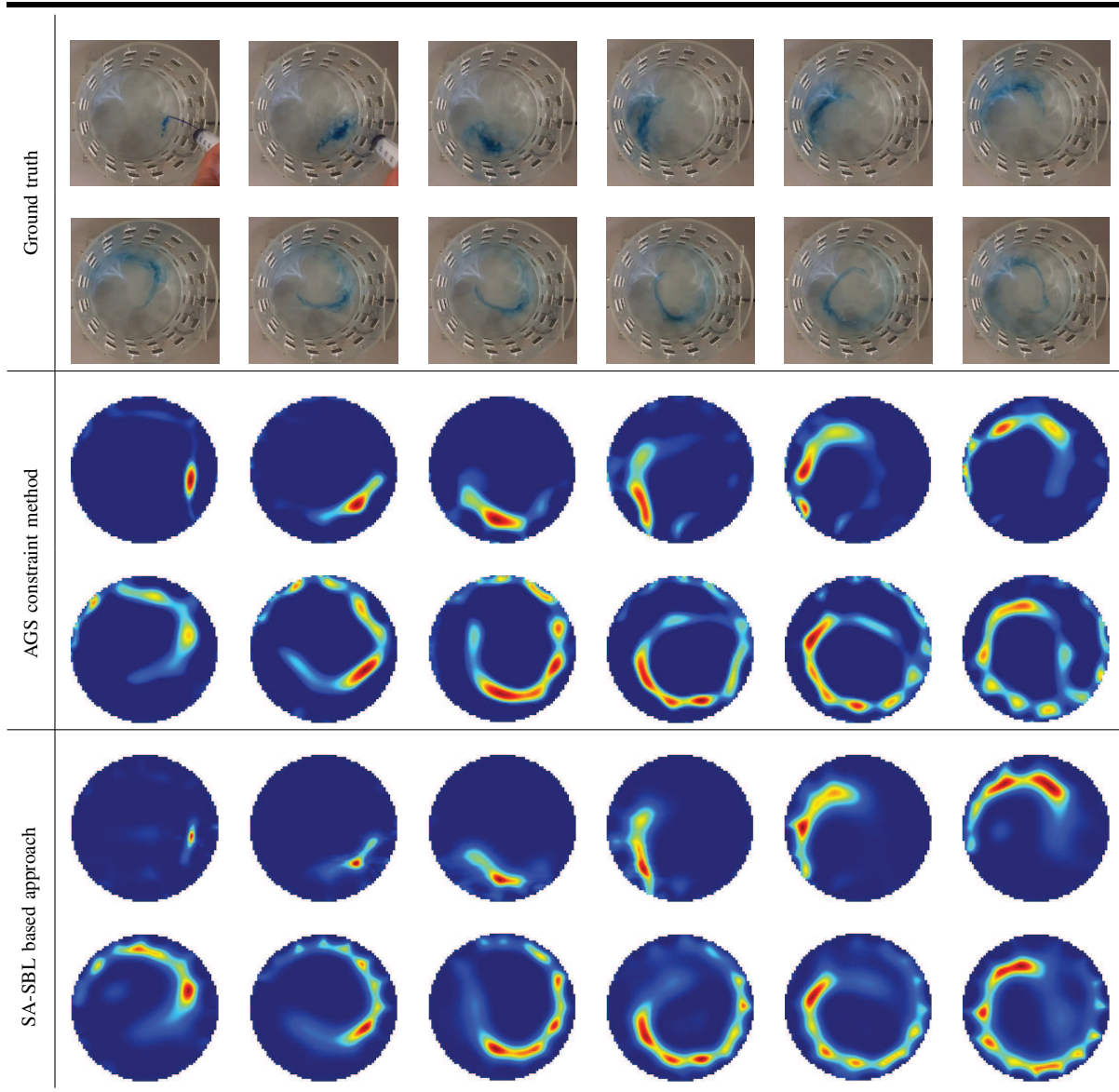
perspective for imaging objects with a low contrast.

V. CONCLUSION

The objective of this paper is to develop a novel algorithm to obtained enhanced EIT image reconstruction by exploiting the structured sparsity in the conductivity distribution. We redesign the existing SBL algorithm by taking into account the pattern coupling between adjacent columns that are not directly neighbored in the target vector. Compared with the existing state-of-the-art algorithms, the proposed method achieves a higher spatial resolution. In addition, since the EIT imaging problem is formulated in a full Bayesian framework, cumbersome parameter tuning process is avoided.

REFERENCES

[1] S.-H. Liu, J. Jia, and Y. Yang, "Image reconstruction algorithm for electrical impedance tomography based on block sparse Bayesian learning," in *Proc. 2017 IEEE Int. Conf. Imaging Syst. Techni. (IST)*, Beijing, China, Oct. 2017.

[2] H. S. Tapp, A. J. Peyton, E. K. Kemsley, and R. H. Wilson, "Chemical engineering applications of electrical process tomography," *Sens. Actuators, B*, vol. 92, no. 1, pp. 17–24, July 2003.

[3] A. Seppänen, A. Voutilainen, and J. P. Kaipio, "State estimation in process tomography—reconstruction of velocity fields using EIT," *Inverse Prob.*, vol. 25, no. 8, pp. 085009, July 2009.

[4] J. Jia, M. Wang, H. I. Schlaberg, and H. Li, "A novel tomographic sensing system for high electrically conductive multiphase flow measurement," *Flow Meas. Instrum.*, vol. 21, no. 3, pp. 184-190, Sept. 2010.

[5] P. Church, J. E. Mcfee, S. Gagnon, and P. Wort, "Electrical impedance tomographic imaging of buried landmines," *IEEE Trans. Geosci. Remote Sens.*, vol. 44, no. 9, pp. 2407–2420, Sept. 2006.

[6] E. Zimmermann, A. Kemna, J. Berwix, W. Glaas, and H. Vereecken, "EIT measurement system with high phase accuracy for the imaging of spectral induced polarization properties of soils and sediments," *Meas. Sci. Technol.*, vol. 19, no. 9, pp. 094010, July 2008.

[7] G. Bouchette, P. Church, J. E. Mcfee, and A. Adler, "Imaging of compact objects buried in underwater sediments using electrical impedance tomography," *IEEE Trans. Geosci. Remote Sens.*, vol. 52, no. 2, pp. 1407–1417, Feb. 2014.

[8] T. Tidswell, A. Gibson, R. H. Bayford, and D S. Holder, "Three-dimensional electrical impedance tomography of human brain activity," *NeuroImage*, vol. 13, no. 2, pp. 283–294, Feb. 2001.

[9] M. T. Clay, and T. C. Ferree, "Weighted regularization in electrical impedance tomography with applications to acute cerebral stroke," *IEEE Trans. Med. Imaging*, vol. 21, no. 6, pp. 629–637, June 2002.

[10] R. J. Halter, A. Hartov, and K. D. Paulsen, "A broadband high-frequency electrical impedance tomography system for breast imaging," *IEEE Trans. Biomed. Eng.*, vol. 55, no. 2, pp. 650–659, Feb. 2008.

[11] A. Adler and R. Guardo, "Electrical impedance tomography: Regularized imaging and contrast detection," *IEEE Trans. Med. Imaging*, vol. 15, no. 2, pp. 170–179, Apr. 1996.

[12] J. P. Kaipio, V. Kolehmainen, M. Vauhkonen, and E. Somersalo, "Inverse problems with structural prior information," *Inverse Prob.*, vol. 15, no. 3, pp. 713–729, Mar. 1999.

[13] Y. Yang, J. Jia, N. Polydorides, and H. McCann, "Effect of structured packing on EIT image reconstruction," in *Proc. IEEE Int. Conf. Imaging Syst. Tech.*, Santorini, Greece, pp. 53–58, Oct. 2014.

[14] W.-Q. Yang, D. M. Spink, T. A. York, and H. McCann, "An image reconstruction algorithm based on Landweber's iteration method for electrical capacitance tomography," *Meas. Sci. Technol.*, vol. 10, no. 11, pp. 1065-1069, Nov. 1999.

[15] H.-X. Wang, C. Wang, and W.-L. Yin, "A pre-iteration method for the inverse problem in electrical impedance tomography," *IEEE Trans. Instrum. Meas.*, vol. 53, no. 4, pp. 1093–1096, Aug. 2004.

[16] T. Li, T.-J. Kao, D. Isaacson, J. C. Newell, and G. J. Saulnier, "Adaptive Kaczmarz method for image reconstruction in electrical impedance tomography," *Physiol. Meas.*, vol. 34, no. 6, pp. 595-608, May 2013.

[17] Y. Z. Ider and S. Onart, "Algebraic reconstruction for 3D magnetic resonanceelectrical impedance tomography (MREIT) using one component of magnetic flux density," *Physiol. Meas.*, vol. 25, no. 1, pp. 281–294, Feb. 2004.

[18] A. Borsic, B. M. Graham, A. Adler, and W. R. Lionheart, "*In vivo* impedance imaging with total variation regularization," *IEEE Trans. Med. Imaging*, vol. 29, no. 1, pp. 44–54, Jan. 2010.

[19] Z. Zhou, G. S. dos Santos, T. Dowrick, J. Avery, Z.-L. Sun, H. Xu, and D. S. Holder, "Comparison of total variation algorithms for electrical impedance tomography," *Physiol. Meas.*, vol. 36, no. 6, pp. 1193–1209, May 2015.

[20] T. Dai and A. Adler, "Electrical impedance tomography reconstruction using ℓ_1 norms for data and image terms," in *Proc. 30th Annu. Int. Conf. IEEE EMBS*, Vancouver, BC, Canada, pp. 2721–2724, Aug. 2008.

[21] J. N. Tehrania, A. McEwana, C. Jin, and A. van Schaikb, "$L1$ regularization method in electrical impedance tomography by using the $L1$-curve (Pareto frontier curve)," *Appl. Math. Modell.*, vol. 36, no. 3, pp. 1095–1105, Mar. 2012.

[22] M. Gehre, T. Kluth, A. Lipponen, B. Jin, A. Seppänen, J. P. Kaipio, and P. Maass, "Sparsity reconstruction in electrical impedance tomography: an experimental evaluation," *J. Comput. Appl. Math.*, vol. 236, no. 8, pp. 2126–2136, Feb. 2012.

[23] Y. C. Eldar, P. Kuppinger, and H. Bolcskei, "Block-sparse signals: Uncertainty relations and efficient recovery," *IEEE Trans. Signal Process.*, vol. 58, no. 6, pp. 3042–3054, June 2010.

[24] Y. Yang and J. Jia, "An image reconstruction algorithm for electrical impedance tomography using adaptive group sparsity constraint," *IEEE Trans. Instrum. Meas.*, vol. 66, no. 9, pp. 2295–2305, Sept. 2017.

[25] J. Kaipio and E. Somersalo, *Statistical and Computational Inverse Problems*. Springer Science & Business Media, 2006.

[26] A. M. Stuart, "Inverse problems: A Bayesian perspective," *Acta Numerica*, vol. 19, pp. 451–559, May 2010.

[27] J. P. Kaipio, V. Kolehmainen, E. Somersalo, and M. Vauhkonen, "Statistical inversion and Monte Carlo sampling methods in electrical impedance tomography," *Inverse Prob.*, vol. 16, no. 5, pp. 1487–1522, Oct. 2000.

[28] J. Martin, L. C. Wilcox, C. Burstedde, and O. Ghattas, "A stochastic Newton MCMC method for large-scale statistical inverse problems with application to seismic inversion," *SIAM J. Sci. Comput.*, vol. 34, no. 3, pp. A1460–A1487, June 2012.

[29] V. H. Hoang, C. Schwab, and A. M. Stuart, "Complexity analysis of accelerated MCMC methods for Bayesian inversion," *Inverse Prob.*, vol. 29, no. 8, pp. 085010, July 2013.

[30] D. Calvetti, and E. Somersalo, "A Gaussian hypermodel to recover blocky objects," *Inverse Prob.*, vol. 23, no. 2, pp. 733–754, Mar. 2007.

[31] D. Calvetti, and E. Somersalo, "Hypermodels in the Bayesian imaging framework," *Inverse Prob.*, vol. 24, no. 3, pp. 034013, May 2008.

[32] D. Calvetti, H. Hakula, S. Pursiainen, and E. Somersalo, "Conditionally Gaussian hypermodels for cerebral source localization," *SIAM J. Imag. Sci.*, vol. 2, no. 3, pp. 879–909, July 2009.

[33] M. Lassas, E. Saksman, and S. Siltanen, "Discretization-invariant Bayesian inversion and Besov space priors," *Inverse Prob. Imaging*, vol. 3, no. 1, pp. 87–122, Jan. 2009.

[34] V. Kolehmainen, M. Lassas, K. Niinimäki, and S. Siltanen, "Sparsity-promoting Bayesian inversion," *Inverse Prob.*, vol. 28, no. 2, pp. 025005, Jan. 2012.

[35] T. Bui-Thanh and O. Ghattas, "A scalable algorithm for MAP estimators in Bayesian inverse problems with Besov priors," *Inverse Prob. Imaging*, vol. 9, no. 1, pp. 27–53, Jan. 2015.

[36] L. Roininen, J. Huttunen, and S. Lasanen, "Whittle-Matérn priors for Bayesian statistical inversion with applications to electrical impedance tomography," *Inverse Prob. Imaging*, vol. 8, no. 2, pp. 561–586, May 2014.

[37] L. Harhanen, N. Hyvönen, H. Majander, and S. Staboulis, "Edge-enhancing reconstruction algorithm for three-dimensional electrical impedance tomography," *SIAM J. Sci. Comput.*, vol. 37, no. 1, pp. B60–B78, Jan. 2015.

[38] D. Calvetti, A. Pascarella, F. Pitolli, E. Somersalo, and B. Vantaggi, "A hierarchical Krylov-Bayes iterative inverse solver for MEG with physiological preconditioning," *Inverse Prob.*, vol. 31, no. 12, pp. 125005, Dec. 2015.

[39] Z.-L. Zhang and B. D. Rao, "Extension of SBL algorithms for the recovery of block sparse signals with intra-block correlation," *IEEE Trans. Signal Process.*, vol. 61, no. 8, pp. 2009–2015, Apr. 2013.

[40] J. Fang, Y.-N. Shen, H.-B. Li, and P. Wang, "Pattern-coupled sparse Bayesian learning for recovery of block-sparse signals," *IEEE Trans. Signal Process.*, vol. 63, no. 2, pp. 360–372, Jan. 2013.

[41] Q. Wu, Y. D. Zhang, M. G. Amin, and B. Himed, "Multi-task Bayesian compressive sensing exploiting intra-task dependency," *IEEE Signal Process. Lett.*, vol. 22, no. 4, pp. 430–434, Apr. 2015.

[42] S.-H. Liu, Y. D. Zhang, T. Shan, S. Qin, and M. G. Amin, "Structure-aware Bayesian compressive sensing for frequency-hopping spectrum estimation," in *Proc. SPIE 9857, Compressive Sensing V: From Diverse Modalities to Big Data Analytics*, Baltimore, MD, USA, pp. 98570N, May 2016.

[43] S.-H. Liu, Y. D. Zhang, and T. Shan, "Detection of weak astronomical signals with frequency-hopping interference suppression," *Digital Signal Process.*, vol. 72, pp. 1–8, Jan. 2018.

[44] S.-H. Liu, Y. D. Zhang, T. Shan, and R. Tao, "Structure-aware Bayesian compressive sensing for frequency-hopping spectrum estimation with missing observations," *IEEE Trans. Signal Process.*, vol. 66, no. 8, pp. 2153–2166, Apr. 2018.

[45] E. Somersalo, M. Cheney, and D. Isaacson, "Existence and uniqueness for electrode models for electric current computed tomography," *SIAM J. Appl. Math.*, vol. 52, no. 4, pp. 1023–1040, Aug. 1992.

[46] N. Polydorides and W. R. B. Lionheart, "A Matlab toolkit for three-dimensional electrical impedance tomography: A contribution to the electrical impedance and diffuse optical reconstruction software project," *Meas. Sci. Technol.*, vol. 13, no. 12, pp. 1871–1883, Dec. 2002.

[47] P. J. Vauhkonen, M. Vauhkonen, T. Savolainen, and J. P. Kaipio, "Three-dimensional electrical impedance tomography based on the complete electrode model," *IEEE Trans. Biomed. Eng.*, vol. 46, no. 9, pp. 1150-1160, Sept. 1999.

[48] P. Stoica and P. Babu, "SPICE and LIKES: Two hyperparameter-free methods for sparse-parameter estimation," *Signal Process.*, vol. 92, no. 7, pp. 1580–90, July 2012.

[49] A. Nissinen, L. M. Heikkinen, and J. P. Kaipio, "The Bayesian approximation error approach for electrical impedance tomography — experimental results," *Meas. Sci. Technol.*, vol. 19, no. 1, pp. 015501, Jan. 2008.

[50] H.-T. Li, R.-Q. Chen, C.-H. Xu, B.-Y. Liu, M.-X. Tang, and Y. Lin, "Unveiling the development of intracranial injury using dynamic brain EIT: An evaluation of current reconstruction algorithms," *Physiol. Meas.*, vol. 38, no. 9, pp. 1776–1790, Sept. 2017.

[51] D. L. Donoho and M. Elad, "Optimally sparse representation in general (nonorthogonal) dictionaries via ℓ_1 minimization," *Proc. Nat. Aca. Sci.*, vol. 100, no. 5, pp. 2197-2202, Mar. 2003.

[52] M. Vauhkonen, D. Vadász, P. A. Karjalainen, E. Somersalo, and J. P. Kaipio, "Tikhonov regularization and prior information in electrical impedance tomography," *IEEE Trans. Med. Imaging*, vol. 17, no. 2, pp. 285–293, Apr. 1998.

[53] I. Markovsky and S. Van Huffel, "Overview of total least-squares methods," *Signal Process.*, vol. 87, no. 10, pp. 2283–2302, Oct. 2007.

[54] M. Brischwein, S. Herrmann, W. Vonau, F. Berthold, H. Grothe, E. R. Motrescu, and B. Wolf, "Electric cell-substrate impedance sensing with screen printed electrode structures," *Lab Chip*, vol. 6, no. 6, pp. 819–822, Apr. 2006.

[55] D. Koley and A. J. Bard, "Triton X-100 concentration effects on membrane permeability of a single HeLa cell by scanning electrochemical microscopy (SECM)," *Proc. Natl. Acad. Sci.*, vol. 107, no. 39, pp. 16783–16787, Aug. 2010.

[56] C. Gabriel, S. Gabriel, and E. Corthout, "The dielectric properties of biological tissues: I. Literature survey," *Phys. Med. Biol.*, vol. 41, no. 11, pp. 2231–2249, Nov. 1996.

[57] O. Gilad and D. S. Holder, "Impedance changes recorded with scalp electrodes during visual evoked responses: Implications for electrical impedance tomography of fast neural activity," *NeuroImage*, vol. 47, no. 2, pp. 514–522, Aug. 2009.

[58] K. Y. Aristovich, B. C. Packham, H. Koo, G. Sato dos Santos, A. McEvoy, and D. S. Holder, "Imaging fast electrical activity in the brain with electrical impedance tomography," *NeuroImage*, vol. 124, no. 1, pp. 204–213, Jan. 2016.

[59] A. D. Liston, R. H. Bayford, and D. S. Holder, "The effect of layers in imaging brain function using electrical impedance tomograghy," *Physiol. Meas.*, vol. 25, no. 1, pp. 143–158, Feb. 2004.

[60] A. Romsauerova, A. McEwan, L. Horesh, R. Yerworth, R. H. Bayford, and D. S. Holder, "Multi-frequency electrical impedance tomography (EIT) of the adult human head: initial findings in brain tumours, arteriovenous malformations and chronic stroke, development of an analysis method and calibration," *Physiol. Meas.*, vol. 27, no. 5, pp. S147–S161, Apr. 2006.

[61] J. Malmivuo and R. Plonsey, *Bioelectromagnetism: Principles and Applications of Bioelectric and Biomagnetic Fields*. Oxford University Press, 1995.

[62] E. Malone, M. Jehl, S. Arridge, T. Betcke, and D. S. Holder, "Stroke type differentiation using spectrally constrained multifrequency EIT: Evaluation of feasibility in a realistic head model," *Physiol. Meas.*, vol. 35, no. 6, pp. 1051–1066, May 2014.

[63] A. Boyle and A. Adler, "The impact of electrode area, contact impedance and boundary shape on EIT images," *Physiol. Meas.*, vol. 32, no. 7, pp. 745–754, June 2011.